



## Article

# One-Pot Environmentally Friendly Synthesis of Nanomaterials Based on Phytate-Coated Fe<sub>3</sub>O<sub>4</sub> Nanoparticles for Efficient Removal of the Radioactive Metal Ions <sup>90</sup>Sr, <sup>90</sup>Y and (UO<sub>2</sub>)<sup>2+</sup> from Water

Paulino Duel, María de las Nieves Piña \* and Jeroni Morey \*

Departament de Química, Universitat de les Illes Balears, Cra. de Valldemossa km 7.5, 07122 Palma de Mallorca, Spain

\* Correspondence: neus.pinya@uib.es (M.d.l.N.P.); jeroni.morey@uib.es (J.M.)

**Abstract:** We report the fast (three minutes) synthesis of green nanoparticles based on nanoparticles coated with the natural organic receptor phytate for the recognition and capture of <sup>90</sup>Sr, <sup>90</sup>Y, and (UO<sub>2</sub>)<sup>2+</sup>. The new material shows excellent retention for (UO<sub>2</sub>)<sup>2+</sup>, 97%; these values were 73% and 100% for <sup>90</sup>Sr and <sup>90</sup>Y, respectively. Recovery of the three radioactive metal ions occurs through a non-competitive process. The new hybrid material is harmless, easy to prepare, and immobilizes these radioactive contaminants in water with great efficiency.

**Keywords:** adsorption removal; radioactive metal ions; magnetite nanoparticles; phytate; one-pot synthesis; water contamination



**Citation:** Duel, P.; Piña, M.d.l.N.; Morey, J. One-Pot Environmentally Friendly Synthesis of Nanomaterials Based on Phytate-Coated Fe<sub>3</sub>O<sub>4</sub> Nanoparticles for Efficient Removal of the Radioactive Metal Ions <sup>90</sup>Sr, <sup>90</sup>Y and (UO<sub>2</sub>)<sup>2+</sup> from Water. *Nanomaterials* **2022**, *12*, 4383. <https://doi.org/10.3390/nano12244383>

Academic Editor: Lyudmila M. Bronstein

Received: 17 November 2022

Accepted: 7 December 2022

Published: 9 December 2022

**Publisher's Note:** MDPI stays neutral with regard to jurisdictional claims in published maps and institutional affiliations.



**Copyright:** © 2022 by the authors. Licensee MDPI, Basel, Switzerland. This article is an open access article distributed under the terms and conditions of the Creative Commons Attribution (CC BY) license (<https://creativecommons.org/licenses/by/4.0/>).

## 1. Introduction

The use of nuclear energy, as well as the isolation and handling of radioisotopes in medicine and industry, is one of the greatest achievements of modern science and technology. However, nuclear energy also generates highly polluting and hazardous waste. The world has recently closed many nuclear power plants that generate tons of highly contaminated waste.

The radioactive lifetime of some radioisotopes can be very long. The half-life of uranium is  $2.48 \times 10^5$  years, and it is the largest waste generated by a nuclear power plant; uranium is a highly toxic and carcinogenic waste. The maximum level established by the EPA for the ambient concentration of uranium is 30 µg/L [1].

Yttrium has an abundance in the Earth's crust of 0.0028% [2]. It is used industrially in the construction of lasers, and, together with neodymium, is used to remove tattoos. It is also used with aluminum for the generation of artificial diamonds [3]. The radioactive isotope <sup>90</sup>Y is used for selective internal radiation therapy (SIRT) to treat liver cancers [4,5]. Yttrium is a toxic metal that can damage the eyes and lungs [6]. The maximum concentration allowed in water for human consumption is 6.4 µg/L [7].

Strontium is an essential element in the human body at trace levels. Strontium stimulates the creation of bone material and has been directly related to the compressive strength of bones. Strontium ranelate inhibits bone demineralization in patients with postmenopausal osteoporosis. However, an excess of this metal inhibits bone mineralization. The chemical similarity of Sr<sup>2+</sup> with Ca<sup>2+</sup> causes displacement of calcium from bones leading to malformations or dysfunctions in the skeleton [8]. Sr<sup>2+</sup> absorption can also act with vitamin D to cause adverse effects on the synthesis of 1,25-dihydroxyvitamin D<sub>3</sub>, thus directly affecting the skeleton and causing rickets in animal models [9].

Strontium occurs in nature with different stable isotopes (<sup>84</sup>Sr, <sup>86</sup>Sr, <sup>87</sup>Sr, and <sup>88</sup>Sr). Isotopes <sup>85</sup>Sr, <sup>89</sup>Sr, and <sup>90</sup>Sr are naturally radioactive. <sup>90</sup>Sr is the most dangerous radioactive

isotope with a half-life of 28.79 years. This can cause prolonged beta emission with long exposure times.  $^{90}\text{Sr}$  decay generates radioisotope  $^{90}\text{Y}$  that subsequently decays to  $^{90}\text{Zr}$  as a stable isotope. The half-life of yttrium-90 is 64.1 h. It is a high-energy  $\beta$ -emitter ( $E_{\text{max}} = 2.27 \text{ MeV}$ ) [10], and it emits beta radiation faster than  $^{90}\text{Sr}$ . Radioactive strontium is generated by nuclear fission in the explosion of nuclear weapons or during accidents in nuclear plants. It is generated mostly as  $^{90}\text{Sr}$  to generate particles with other components ( $<1 \mu\text{m}$ ) that can travel worldwide depending on their size. The accumulation of  $^{90}\text{Sr}$  in bones leads to direct exposure of bone and muscle cells to beta radiation, thus causing DNA deterioration and generating cancer cells [11]. To summarize, U(VI),  $^{90}\text{Sr}$ , and  $^{90}\text{Y}$  are persistent and very toxic contaminants. Thus, their controlled storage is a key goal.

Hybrid magnetite nanoparticles have been proposed as an alternative for environmental remediation [12–15] including the removal of noble metal salts (Ag and Au [16]) or salts of heavy metals contaminants such as Hg(II) and Pb(II) [17]. They have also proven useful in the capture of polycyclic aromatic hydrocarbons (PAHs) [18]. More recently, hybrid magnetite nanoparticles are used in the quantitative determination of volatile organic compounds (VOCs) [19].

All this is the result of the low cost and the great versatility in the preparation of hybrid magnetite nanoparticles, which are coordinated with different organic remains and can join with different target molecules. The contaminant is generally dissolved or is present in water. The inherent magnetism of hybrid magnetite nanoparticles offers simple and effective removal of the contaminant from the sample by magneto filtration once coordinated on its surface. This obviates the need to use external filters. Magnetism also allows one to concentrate the complex formed by the association of hybrid magnetite nanoparticles with the analyte. This leads to greater control over the captured analyte and is a particularly promising solution to collect and store highly toxic and dangerous radioactive substances. One can then store and maintain them in a monitored environment.

The phosphonate group can form a strong bond with the surface of  $\text{Fe}_3\text{O}_4$  nanoparticles (FeNPs). This process coats their surface and protects them from oxidation of Fe(II) to Fe(III) [20] and prevents their lixiviation. The phosphate group also effectively coordinates with the salts of uranium U(VI), Sr(II), and Y(III) [21–25].

Phytate is a natural and economical source of phosphate groups. Phytate is a natural product produced by plants and serves as a reserve of *myo*-inositol and phosphates for plants. Chemically, phytate is the dihydrogen phosphate ester of *myo*-inositol, or *cis*-1,2,3,5-*trans*-4,6-cyclohexanehexol. The most abundant and thermodynamically stable conformer has five groups of the six phosphates in equatorial positions (1a5e) [26]. However, the molecule can reverse the orientation from equatorial to axial (5a1e) at a pH between 9.0–9.5 [27,28].

Here, we present an efficient single-step synthesis of magnetite nanoparticles coated with phytate (Phy@ $\text{Fe}_3\text{O}_4$ ). This method is simple and fast ( $<3 \text{ min}$ ) and does not require the use of organic solvents. Only water is required and there are no special reaction conditions (anhydrous reagents, inert atmosphere, or controlled temperature or catalysts). The Phy@ $\text{Fe}_3\text{O}_4$  show excellent uranium uptake: approximately 950 milligrams of uranium per milligram of Phy@ $\text{Fe}_3\text{O}_4$  in aqueous samples of 100 ppm uranium. These were made under normal environmental conditions and show a high affinity for salts of  $^{90}\text{Y}$ (III) and  $^{90}\text{Sr}$ (II) [29].

## 2. Materials and Methods

### 2.1. Reagents

All commercially available reagents were of analytical grade. Inositol hexaphosphoric acid sodium salt (phytic acid sodium salt hydrate) from rice, strontium standard for ICP TraceCERT<sup>®</sup>  $\text{HNO}_3$  2% w/w, yttrium standard for ICP TraceCERT<sup>®</sup>  $\text{HNO}_3$  2% w/w, and uranium ICP standard  $\text{UO}_2(\text{NO}_3)_2 \cdot 6\text{H}_2\text{O}$  in  $\text{HNO}_3$  2–3% 10 mg/L U were purchased from Sigma-Aldrich (Waltham, MA, USA). All solvents were purchased from Scharlau and Fisher Chemicals. Acros Organics supplied iron (II) chloride tetrahydrate ( $\text{FeCl}_2 \cdot 4\text{H}_2\text{O}$ ) and iron

(III) chloride (FeCl<sub>3</sub> anhydrous). High purity water was generated by Milli-Q apparatus (Millipore Corp., Madrid, Spain).

## 2.2. Characterization of the Nanomaterials

Reactions and the sorption experiments used oven-dried glassware. The nanomaterials were characterized with optical, thermal, spectroscopic, and microscopic techniques.

Infrared spectra (FT-IR) analysis of samples used a Bruker Tensor 27 instrument (Bruker Española, Madrid, Spain) by mixing dried Phy@Fe<sub>3</sub>O<sub>4</sub> powders into KBr pellets. The spectra were collected with a resolution of 4 cm<sup>-1</sup> from 4000–400 cm<sup>-1</sup>.

Thermogravimetric analysis (TGA) used a SDT Q600 TA (TA Instruments, New Castle, DE, USA) in Al<sub>2</sub>O<sub>3</sub> crucibles. Dried samples (typically 7–8 mg) were initially held at 40 °C for 10 min before heating to 600 °C at a rate of 10 °C min<sup>-1</sup> in an N<sub>2</sub> atmosphere.

Inductively coupled plasma-optical emission spectrometry (ICP-OES) was performed on a Perkin-Elmer Optima 5300 DV instrument (Thermo Fisher Scientific, Waltham, MA, USA).

Transmission electron microscopy (TEM) used a Philips Jeol JEM 2100F (Jeol, Zurich, Switzerland). A drop of the different nanoparticle suspensions was drop-cast on a copper TEM grid with a carbowax backing.

Size and zeta potential were measured via dynamic light scattering (DLS) with a Malvern Zetasizer Nano ZS (Malvern Panalytical, Malvern, UK) at 25 °C.

A NdBF<sub>e</sub> neodymium magnet (60 mm × 30 mm × 15 mm and 549.4 M of maximum magnetic force) was from Supermagnete (Gottmadingen, Germany). A flatbed orbital shaker IKA VXR basic Vibrax was also used (IKA-Werke GmbH & Co. KG, Staufen, Germany).

Bremsstrahlung radiation from <sup>90</sup>Y(III) was measured using a LB4200 Alpha-Beta radioisotope dose calibrator (Mirion Technologies, Canberra, Inc. Meriden, CT, USA). All measurements were performed under the same geometric conditions. The results are reported as the mean of at least three measurements ± standard deviation.

## 2.3. Quantification of Residual Metal Concentrations Using ICP-OES

The number of remaining cations in the solution after different mixing times were measured by ICP-OES. Here, an acid solution (HNO<sub>3</sub> 2%) of all cations at a concentration of 1000 ppb was used. The ICP-OES was calibrated just before each measurement between 0 to 1000 ppb. The Phy@Fe<sub>3</sub>O<sub>4</sub> were previously sonicated for 10–20 min to achieve a good dispersion.

In a 12 mL Falcon tube, 10 mL of a metal salt solution (1000 ppb) was introduced, followed by 0.5 mL of a suspension of functionalized phytate magnetic nanoparticles in milli-Q water. The amount of Phy@Fe<sub>3</sub>O<sub>4</sub> depends on the concentration of the suspension and was precalculated. This mixture was stirred for two hours. The suspension was then decanted using an NdBF<sub>e</sub> magnet, and the supernatant was filtered with a 0.45-micrometer filter to confirm that no nanoparticles entered the instrument. The elimination efficiency and the adsorption capacity at equilibrium,  $q_m$  (mg/g), were calculated as follows using the data obtained in these experiments (see Equations).

$$\text{Removal (\%)} = [(C_o - C_t)/C_o] \times 100\%$$

$$q_m = (C_o - C_e) V / m$$

The  $C_o$  (mol/L) is the initial concentration of metallic salt,  $C_t$  (mol/L) is the concentration of metallic salt after adsorption at time  $t$ , and  $C_e$  (mg/L) is the equilibrium concentration.  $V$  (L) is the volume of the solution used for the extraction experiment and  $m$  is the mass of nanoparticles used in the experiments, expressed in grams.

#### 2.4. Quantification of Residual $^{90}\text{Sr}/^{90}\text{Y}$ Activity

A solution of  $^{90}\text{Sr}/^{90}\text{Y}$  in equilibrium was used. The results initially showed a standard activity of  $99.49 \pm 0.2$  Bq/g (15 October 1998). On the day of the experiment, 10 May 2021, the recorded activity was 57.88 Bq/g. Measurements were made using 4.84 g of this standard solution dissolved in 20 mL of milli-Q water at pH 6.5. The standard solution (20 mL) was divided into four 10-mL glass tubes. The total activity measured was 280.14 Bq.

Next, 2.5 mg of  $\text{Phy}@Fe_3O_4$  were added to each tube. The samples were shaken in an orbital flatbed shaker for 2 h. The  $\text{Phy}@Fe_3O_4$  were then collected from each aliquot using an NdBFe magnet. From each aliquot, 3 mL of the supernatant solution was extracted and poured onto an aluminum plate. The sample was dried in an oven at  $120^\circ\text{C}$ , and the radioactive activity was then measured for each of the four dry wastes. This measure corresponds to the remaining activity of the solution.

Next, the activity of each aliquot of the decanted  $\text{Phy}@Fe_3O_4$  nanoparticles was measured. The nanoparticles were dispersed with the remaining 2 mL of the solution and filtered with a 0.2-micron PVDF filter. The filter contained the  $\text{Phy}@Fe_3O_4$  nanoparticles coated with  $^{90}\text{Sr}/^{90}\text{Y}$ ; they were dried in an oven set to  $120^\circ\text{C}$ . The radioactivity of the four dry wastes was then measured separately. The measurement of the remaining activity indicates the retention capacity of the nanomaterial in each aliquot.

#### 2.5. Synthesis of $Fe_3O_4$ and $\text{Phy}@Fe_3O_4$ Nanoparticles

##### 2.5.1. Synthesis of $Fe_3O_4$ Nanoparticles

A solution of NaOH 1 M (7 mL) was added to a stirred solution of  $FeCl_3$  (162 mg, 1 mmol) and  $FeCl_2 \cdot 4H_2O$  (100 mg, 0.5 mmol) in Milli-Q water (5 mL) over 15–20 min under argon. When the addition was finished, the mixture was stirred for another 20 min. The black precipitate was collected by a NdBFe neodymium magnet and washed with Milli-Q water until the pH was neutral. Finally, nanoparticles were cleaned with methanol to remove water and suspended in 10 mL of methanol.

##### 2.5.2. Synthesis of $\text{Phy}@Fe_3O_4$ Nanoparticles

200 mg of  $FeCl_2 \cdot 4H_2O$  (1.0 mmol), 320 mg of  $FeCl_3$  (2.0 mmol), and 400 mg of the phytic acid sodium salt (0.61 mmol) were dissolved in Milli-Q water (30 mL). A white precipitate was formed corresponding to the iron phytate salts. Next, 20 mL of NaOH (1 M) solution were added to the suspension, and the reaction was stirred for three minutes at  $25^\circ\text{C}$ . The supernatant of the reaction was clear, and the black power was decanted using a NdBFe neodymium magnet. The product was cleaned with Milli-Q water ( $3 \times 15$  mL) and dried at  $80^\circ\text{C}$ . Once dried, the  $\text{Phy}@Fe_3O_4$  nanoparticles were milled to a fine powder and stored in a closed flask. The  $\text{Phy}@Fe_3O_4$  nanoparticles were stable for at least three months (Figure 1).

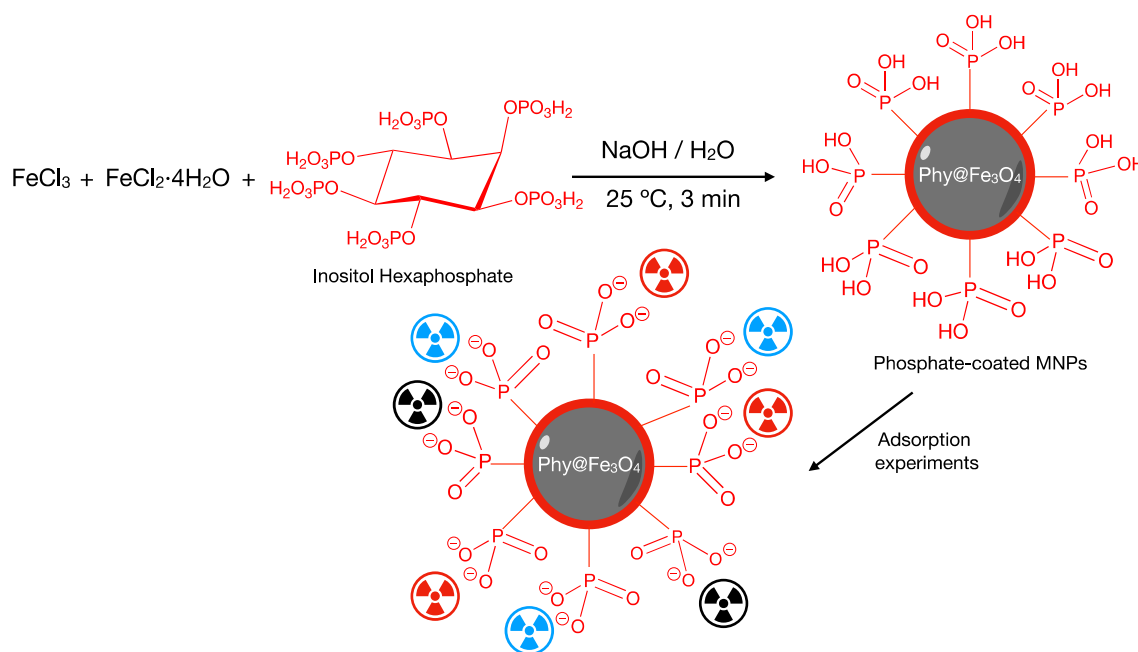


**Figure 1.** Scheme of the procedure of synthesis and functionalization of the magnetite nanoparticles with phytate. Schematic illustration on the adsorption mechanism.

### 3. Results

#### 3.1. Characterization of Magnetite Nanoparticles

The co-precipitation method is a simple, fast, and affordable way to synthesize magnetic iron oxide nanoparticles ( $\text{Fe}_3\text{O}_4$ NPs) [30]. The synthesis procedure is based on the simultaneous precipitation of iron (II) and iron (III) oxides from the solution of the corresponding chlorides in an aqueous medium. The process is carried out under agitation and it uses a strong base (NaOH) to provide the mixed iron oxide, magnetite ( $\text{Fe}_3\text{O}_4$ ), as nanoparticles, with a size of approximately 40 nm. The stoichiometric reaction is presented below.



The synthesized pristine magnetite nanoparticles were decanted by an external magnetic field (NdBFe neodymium). After washing with abundant Milli-Q water to remove excess NaOH from the medium, the  $\text{Fe}_3\text{O}_4$ NPs were rinsed with MeOH to remove excess water, which could speed up the oxidation process. The nanoparticles were preserved by storing in methanol. Iron oxide nanoparticles were characterized by infrared spectroscopy (FT-IR), thermal analysis (TGA), transmission electron microscopy (TEM), dynamic light scattering (DLS), and zeta potential, consistent with the literature [31]. The  $\text{Fe}_3\text{O}_4$ NPs showed a pseudo-spherical shape with an average size of 41 nm. The TEM (Figure S1) displayed that the distribution of the MNPs was between 32.5 and 50 nm.

The DLS data in Figure S1 was performed at pH 6.5 and it showed that the average hydrodynamic radius of the nanoparticles had a value of 288 nm with a polydispersity index (PDI) of 0.281. A small percentage of magnetite nanoparticles (3.6%) were aggregated with an average value of 4677 nm.

The surface of the magnetite nanoparticles is coated with hydroxyl groups as seen in FT-IR, which impacts the zeta potential. The zeta potential is also dependent on the pH of the environment (Figure S1). At pH 6.5 and  $25\text{ }^\circ\text{C}$ , the zeta potential was  $-21.3\text{ mV}$ .

The FT-IR spectrum of the magnetite nanoparticles is shown in Figure S2. It has the most relevant bands ( $3385\text{ cm}^{-1}$  and  $1626\text{ cm}^{-1}$ ) corresponding to the OH groups on the surface of the nanoparticle and the residual water of the sample. The characteristic bands of the Fe–O–Fe bond are clearly observed at  $576\text{ cm}^{-1}$ .

FT-IR data suggest that the pristine surface of the  $\text{Fe}_3\text{O}_4$ NPs is mainly coated with hydroxyl groups ( $-\text{OH}$ ). The hydroxyls can form hydrogen bonds with water molecules, as confirmed by the thermogravimetric analysis (TGA) of magnetite (Figure S3). Between  $20^\circ\text{C}$  and  $200^\circ\text{C}$ , there is a weight loss of 6.893% due to surface-bound water. Above  $200^\circ\text{C}$ , there is a less significant weight loss (2.661%) due to residual water inside nanoparticles' pores.

### 3.2. Characterization of Magnetite Nanoparticles Functionalized by Phytate Groups

The  $\text{Phy@Fe}_3\text{O}_4$  NPs were prepared in a single three-minute step via vigorous stirring of all its components in basic medium. The new material had a black ferrofluid appearance that was easily precipitated by adding a few mg of NaCl to the solution, thus increasing the ionic strength of the medium. The  $\text{Phy@Fe}_3\text{O}_4$  are stable once dry because they are covered by phytate groups, which prevents leaching. They can be stored for three months without any changes to their properties.

The coating of magnetite by phytate is revealed by comparing the FT-IR spectra of  $\text{Fe}_3\text{O}_4$  NPs (blue curves), phytate salt (green curves), and  $\text{Phy@Fe}_3\text{O}_4$  (red curves); see Figure 2. The new material presents characteristic bands of magnetite nanoparticles including a  $\text{Fe}-\text{O}-\text{Fe}$  bond-stretching band at  $578\text{ cm}^{-1}$ . The small displacement observed (from  $576$  and  $578\text{ cm}^{-1}$ ) suggests that there is little change in the internal structure (core) of the magnetite. The broad band at  $3385\text{ cm}^{-1}$  corresponds to the  $\text{O}-\text{H}$  tension bond and to water molecules that cover the surface of the nanoparticles. The signals at  $1181$ ,  $1045$ , and  $896\text{ cm}^{-1}$  indicate free phytate.  $\text{Phy@Fe}_3\text{O}_4$  has displacement at  $1120$ ,  $1057$ , and  $890\text{ cm}^{-1}$ , which can be assigned to  $\text{P}-\text{O}-\text{Fe}$  and the  $\text{P}-\text{O}$  stretching vibrations. The signal at  $890\text{ cm}^{-1}$  is consistent with the  $\text{P}-\text{O}-\text{H}$  band disappearing in the  $\text{Phy@Fe}_3\text{O}_4$  spectra. There is predominantly monodentate/bidentate binding of phytate to the surfaces of  $\text{Fe}_3\text{O}_4$ NPs [5].

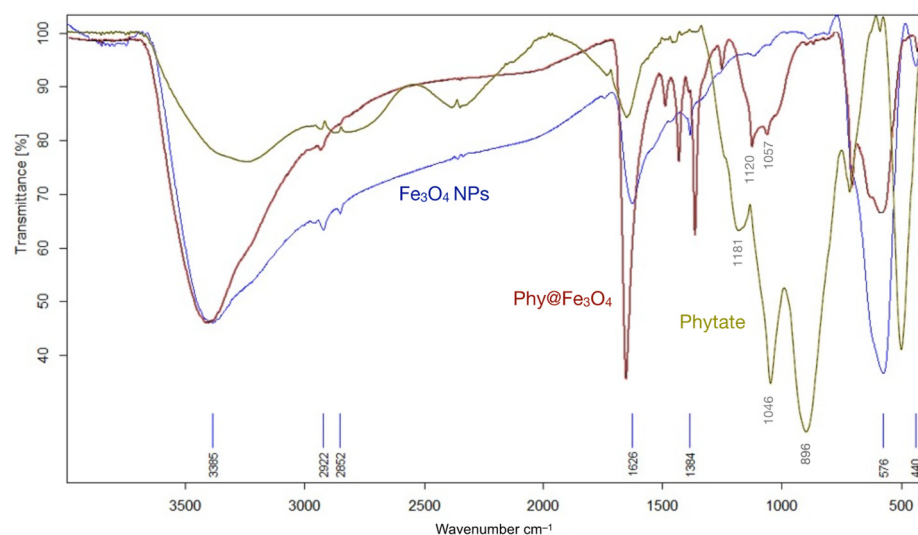


**Figure 2.** Infrared spectra (FT-IR) of different nanomaterials: Magnetite nanoparticles ( $\text{Fe}_3\text{O}_4$ NPs); Phytic acid sodium salt hydrate (Phytate); and magnetite nanoparticles covered with phytate groups ( $\text{Phy@Fe}_3\text{O}_4$ ).

TEM images of the  $\text{Phy@Fe}_3\text{O}_4$  (Figure 3) show a pseudo-spherical morphology with an average size of 110 nm. The size is not homogeneous but it varies between 80 to 160 nm. The average area value is  $38,013\text{ nm}^2$ .

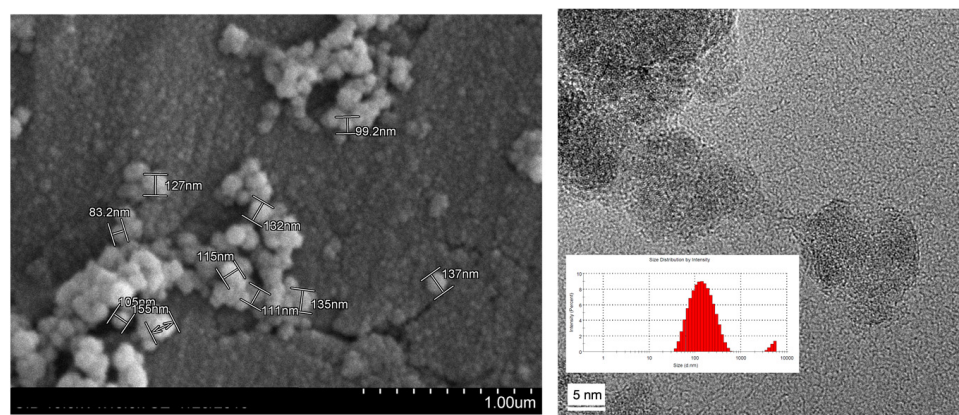


**Figure 3.** TEM micrographs and histogram showing the morphology and particle size distribution of magnetic nanoparticles covered by phytate groups (Phy@Fe<sub>3</sub>O<sub>4</sub>).

Hydrodynamic diameter analysis by DLS was only recorded at pH = 6.09 because this is the approximate pH of the cation samples in the capture experiments. A size distribution between 50 nm and 800 nm was observed, with the average being approximately 196 nm. There is also a small population of fully aggregated particles over 4500 nm.

TGA plots of the Phy@Fe<sub>3</sub>O<sub>4</sub> show a multi-stage mass loss (Figure 4a). The first interval between 80–120 °C can be considered as the loss of water molecules that are weakly bound to the surface of the nanoparticles, which represents 6.17%. The second interval near 200 °C, as well as the third between 270–300 °C, can be considered as the loss of mass corresponding to water molecules strongly bound on the surface of the nanoparticles or associated with hydrogen bonding to phosphate groups. This peak corresponds to a mass loss of 13.30%. Above 300 °C, a mass loss can be seen due to the organic fraction (myo-inositol) of Phy@Fe<sub>3</sub>O<sub>4</sub>. This represents a 4.06% loss and corresponds to the peaks marked by the derivatives located at 436.8 and 473.1 °C. Approximately 30% of phytate, i.e., the fraction of myo-inositol, is consumed by combustion. Thus, it can be assumed that the actual loss of phytate on Phy@Fe<sub>3</sub>O<sub>4</sub> is 26%.

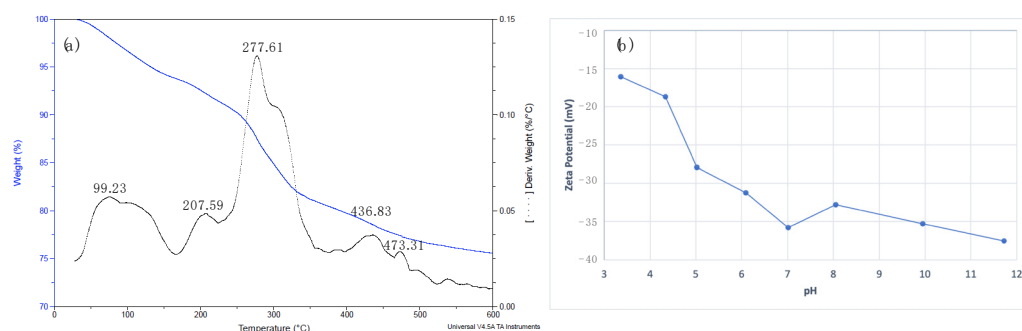


**Figure 4.** (a) TGA diagram of Phy@Fe<sub>3</sub>O<sub>4</sub> nanoparticles under nitrogen atmosphere. (b) z-potential obtained for the Phy@Fe<sub>3</sub>O<sub>4</sub> nanoparticles at different pH.

Phytic acid is a molecule with two different pK<sub>a</sub> values for the 12 acidic protons present. The charge value on the surface of the nanoparticle is highly dependent on the pH of the environment. Figure 4b shows the variation of zeta potential at different pH values in the medium. The zeta potential is always negative from pH 3 to 12; it is near −40 mV above pH 12. From pH 6.8 to 7.2, the zeta potential is around −35 mV suggesting high stability of the suspension of Phy@Fe<sub>3</sub>O<sub>4</sub> nanoparticles. This negative value of the zeta potential suggests that the phosphate groups of the phytate remain at pH 7 and are completely deprotonated.

From the TGA data (mass loss 26%) and TEM (mean radius 110 nm), the number of phytate molecules per nm<sup>2</sup> coordinated with the nanoparticle surface can be determined.

Calculations show that the number of phytate molecules per  $\text{nm}^2$  (insertion coefficient) is 5.6. This insertion coefficient is an indicative measure that suggests that the functionalization of  $\text{Fe}_3\text{O}_4$  nanoparticles is moderate [32].

### 3.3. Magnesium, Calcium, and Strontium Adsorption on Phytate- $\text{Fe}_3\text{O}_4$ NPs

Strontium is an alkaline earth metal that shares chemical-physical similarities with calcium and magnesium. Thus, we studied the retentive capacity of  $\text{Phy@Fe}_3\text{O}_4$  nanoparticles for  $\text{Ca(II)}$ ,  $\text{Sr(II)}$ , and  $\text{Y(III)}$  cations in non-competitive assays, as well as in competitive assays with all cations present in the same aqueous solution. In non-competitive assays, retention studies by  $\text{Phy@Fe}_3\text{O}_4$  nanoparticles were performed separately for each cation. A 10 ppm solution of the cation at pH 7 was treated with 0.5 mg/mL suspended nanoparticles. The resulting suspension was stirred using a vibrating shaker at room temperature for two hours and decanted with a neodymium boron magnet. The remaining concentration of each cation was measured by ICP-OES. The competitive test was performed similarly with 10 ppm of  $\text{Ca(II)}$ ,  $\text{Sr(II)}$ , or  $\text{Y(III)}$  in the initial solution.

In the non-competitive tests (Figure 5), a remarkable retention of the  $\text{Sr(II)}$  (75%) and  $\text{Ca(II)}$  (79%) ions on  $\text{Phy@Fe}_3\text{O}_4$  nanoparticles can be seen. Instead, the  $\text{Phy@Fe}_3\text{O}_4$  nanoparticles only show moderate retention of  $\text{Mg(II)}$  ion (37%).

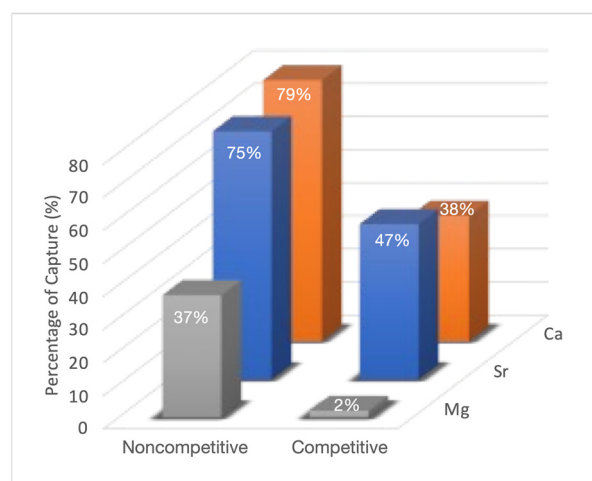


**Figure 5.** ICP-OES percentage retention results obtained by the analysis of 0.5 mg/L of  $\text{Phy@Fe}_3\text{O}_4$  nanoparticles with a 10 ppm of  $\text{Mg(II)}$ ,  $\text{Sr(II)}$  and  $\text{Ca(II)}$  solution in noncompetitive and competitive media.

Competitive tests (Figure 5) show a clear decrease of the retention of all cations by the phytate moiety. While magnesium capture drops to 3%, the retention percentages for  $\text{Ca(II)}$  (38%) and  $\text{Sr(II)}$  (47%) are moderate.

Phosphoric groups in its anionic form establishes strong 1:1 stoichiometry complexes with  $\text{Mg(II)}$ ,  $\text{Ca(II)}$ , and  $\text{Sr(II)}$ .  $\text{Mg(II)}$  has a very stable and totally soluble neutral form at neutral pH (due to its lower ionic radius); thus, it responds to a stoichiometry  $[\text{Mg}_5(\text{H}_2\text{L})]$  where L represents the phytate molecule completely deprotonated.  $\text{Ca(II)}$  and  $\text{Sr(II)}$  have similar species at physiological pH, but they appear in very low concentrations. The solubility products for  $\text{Ca(II)}$  ( $\text{pK}_s = 39.3$ ),  $\text{Sr(II)}$  ( $\text{pK}_s = 35.6$ ), and  $\text{Mg(II)}$  ( $\text{pK}_s = 32.9$ ), indicates that the solubility of the corresponding phytates increases as  $\text{Mg} > \text{Sr} > \text{Ca}$ . This sequence agrees with the retention percentages observed in this study [23].

In a complementary study (Figure S4), it can be observed that keeping the amount of phytate nanoparticles constant (2.5 mg/L) and varying the concentration of  $\text{Sr(II)}$  in the medium from 1 to 20 ppm has no significantly different values of retention, approximately 80%. These data indicate that the equilibrium point has been reached and is marked by the distribution constant.

In parallel, it is proved that the amount of Sr(II) retained depends on the amount of Phy@Fe<sub>3</sub>O<sub>4</sub> nanoparticles used. In Figure S5, this variation is shown by studying 10 ppm of Sr(II) with variable amounts of Phy@Fe<sub>3</sub>O<sub>4</sub> nanoparticles (5.1 mg to 0.32 mg). It is observed that the variation decreases exponentially.

### 3.4. Strontium and Yttrium Adsorption on Phytate-Fe<sub>3</sub>O<sub>4</sub> NPs

It is known that when <sup>90</sup>Sr is released into the environment after an accident, it rapidly decomposes into <sup>90</sup>Y. Therefore, the retention capacity of Phy@Fe<sub>3</sub>O<sub>4</sub> nanoparticles for both Sr(II) and Y(III) cations was studied. The analysis of non-radioactive solutions used an aqueous solution of 10 ppm of each cation at pH 7. Next, 2.5 mg of nanoparticles were introduced into the solution. The suspension was stirred for two hours and collected with a neodymium boron magnet. To fully promote the settling process, the ionic strength of the medium was increased with 50 µL of brine. The remaining concentration of each cation was measured using the ICP-OES. The results obtained shown a retention percentage of 75% for Sr(II) and 100% for Y(III).

The retention capacity of Phy@Fe<sub>3</sub>O<sub>4</sub> nanoparticles was also analyzed with a sample of radioactive strontium. Radioactive strontium contains <sup>90</sup>Sr and <sup>90</sup>Y in equilibrium. Phy@Fe<sub>3</sub>O<sub>4</sub> nanoparticles can separately recognize both metal cations, and the capture of each radioactive cations was determined next: 2.5 mg of Phy@Fe<sub>3</sub>O<sub>4</sub> nanoparticles were added to 5 mL of a standard radioactive solution of 29.7 Bq at pH 6.5. This suspension was stirred using a vibrating shaker at room temperature for 2 h. The Phy@Fe<sub>3</sub>O<sub>4</sub> nanoparticles were then collected with a neodymium-boron magnet. 3 mL of the supernatant solution were removed with a pipette and dried on an aluminum plate at 140 °C. The residue was evaluated with radiometric analysis.

The Phy@Fe<sub>3</sub>O<sub>4</sub> nanoparticles were next dispersed in 2 mL of the solution, and the suspension was filtered with a 0.20-micron PVDF filter to recover the Phy@Fe<sub>3</sub>O<sub>4</sub> nanoparticles. The samples radioactivity was recorded once they were dried on an aluminum plate at 140 °C. This procedure was repeated four times with 5 mL of radioactive solution (Figure 6). The coincidence of results for the uptake of Sr(II) using non-radioactive and radioactive samples is excellent within the experimental error, i.e., 73%, Table 1.

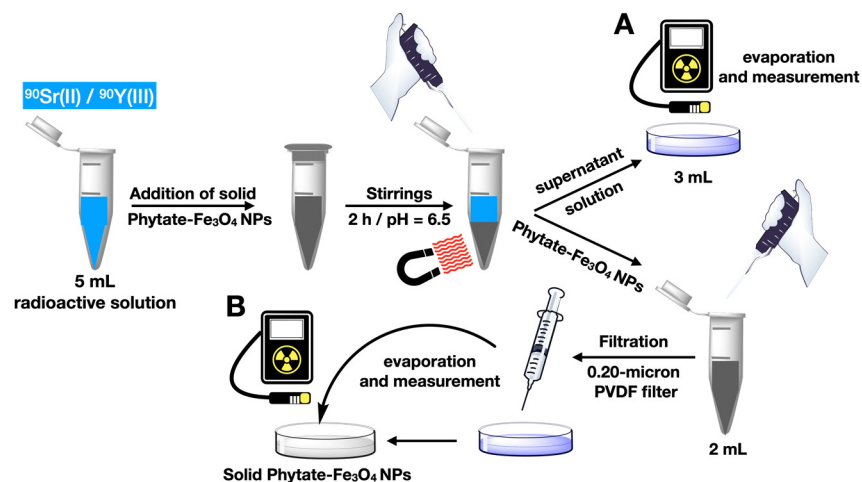


**Figure 6.** Scheme of the methodology followed for the recovery of radioactive strontium and yttrium from a standard sample.

**Table 1.** Results obtained by applying the  $^{90}\text{Sr}$  (II) and  $^{90}\text{Y}$  (III) uptake methodology using  $\text{Phy@Fe}_3\text{O}_4$  nanoparticles.

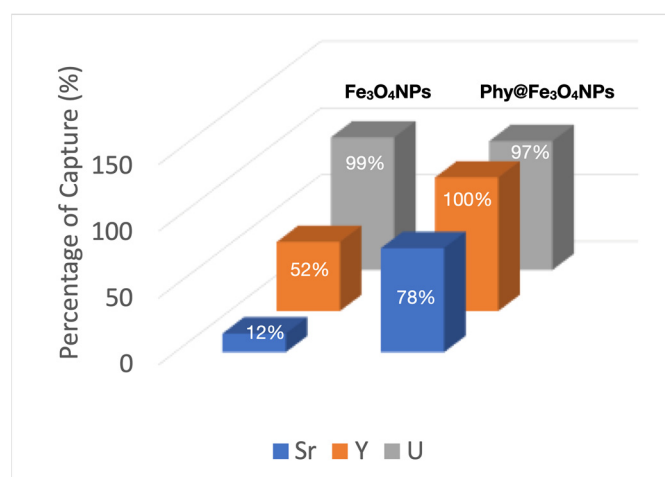
Test	Initial Radioactivity Bq <sup>1</sup>	% Radioactivity Measured in A <sup>2</sup>	% Radioactivity Measured in B <sup>2</sup>	% Total
1	73.43	31	68	99
2	72.75	31	71	102
3	74.00	32	70	102
4	72.19	30	74	104
Average	73.09 ± 0.79	31 ± 0.82	70.75 ± 2.5	101.75 ± 2.06

<sup>1</sup> Bq = Becquerel; <sup>2</sup> See Figure 6.

### 3.5. Uranium Adsorption on $\text{Fe}_3\text{O}_4$ NPs and $\text{Phy@Fe}_3\text{O}_4$ NPs

The isoelectric point of magnetite nanoparticles is in the range of 6.8 to 7.2. At this pH, the uranium species U(VI) that exists in the medium are cationic:  $\text{UO}_2^{2+}$ ,  $\text{UO}_2\text{OH}^+$ , and  $(\text{UO}_2)_3(\text{OH}_5)^+$  [33]. Thus, the sorption of cationic uranium species on amphoteric groups of the magnetite is a favorable process.

As can be seen in Figure 7, the pristine  $\text{Fe}_3\text{O}_4$  NPs show a high uranium uptake activity of almost 100%. This is because  $\text{Fe}_3\text{O}_4$  NPs uptake uranium via adsorption over its negatively charged surface. Then, a redox process then occurs between the Fe(II) to Fe(III) of  $\text{Fe}_3\text{O}_4$  NPs and uranium atoms U(VI)/U(IV) [34].

**Figure 7.** Capture percentages obtained for Sr(II), Y(III) and  $\text{UO}_2^{2+}$  in a competitive test, using  $\text{Fe}_3\text{O}_4$  NPs and  $\text{Phy@Fe}_3\text{O}_4$  NPs.

The pristine  $\text{Fe}_3\text{O}_4$  NPs also show a moderate activity in the uptake of Y(III) (52%) and, to a lesser extent, with the Sr(II) ion; only 12%. There is no doubt that despite showing excellent uranium uptake, the stability of pristine magnetite is precarious because of the oxidation of Fe(II) to Fe(III) that occurs on the surface of the nanoparticle without an adequate coating. This is detrimental to the process.

On the other hand, the  $\text{Phy@Fe}_3\text{O}_4$  NPs show an excellent capacity for the capture of radioactive ions: uranium (VI) (97%), yttrium (III) 100%, and strontium (II) of 78%, in the competitive tests studied. This test was performed by simultaneously adding 5 mL of 1000 ppb of each metal salt to 2.5 mL of 5 mg/L of  $\text{Phy@Fe}_3\text{O}_4$  NPs. This mixture was stirred for two hours at room temperature and pH 6.5. The  $\text{Phy@Fe}_3\text{O}_4$  NPs were then decanted using the NdBFe magnet. 1 mL of the supernatant solution was diluted in 10 mL of  $\text{HNO}_3$  (2%) and analyzed for salt content using ICP-OES.

Moreover, an ICP-OES adsorption study was performed to evaluate the maximum sorption capacity of the  $\text{Phy@Fe}_3\text{O}_4$  NPs as a function of contact time. We analyzed the remaining supernatant concentration of U(VI) at different times (0–200 min). The initial concentration of U(VI) was  $20 \text{ mgL}^{-1}$  in contact with 2.5 mg of  $\text{Phy@Fe}_3\text{O}_4$  NPs. Figure 8

shows that the maximum retention at equilibrium occurs after 2 h and remains constant at longer time points. This test was carried out at pH = 6.5 and 20 °C. The affinity of the Phy@Fe<sub>3</sub>O<sub>4</sub> NPs for the uranyl cation is obvious: After one hour, only ~2 ppm of U(VI) remains in solution, which indicates that already 90% of U(VI) is adsorbed on the Phy@Fe<sub>3</sub>O<sub>4</sub> NPs.

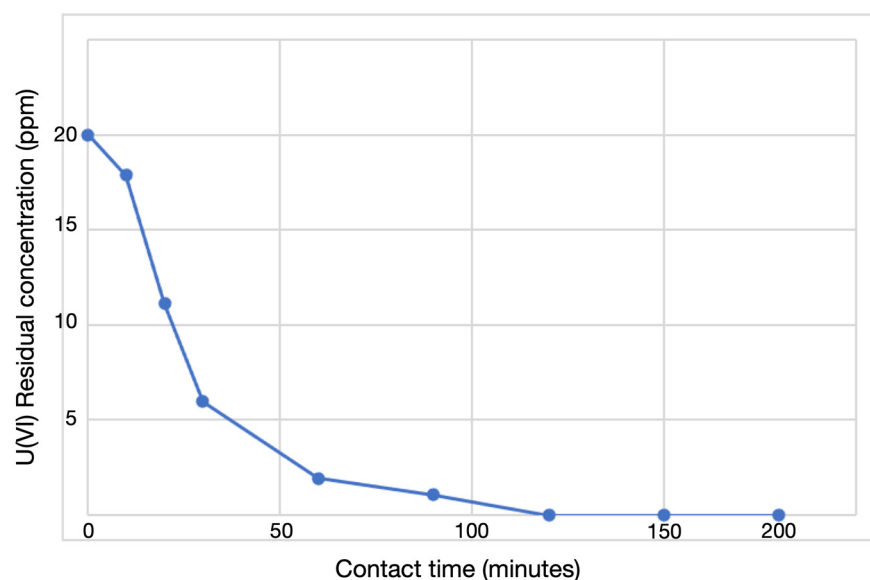


**Figure 8.** ICP-OES data of the supernatants collected after U(VI) adsorption on Phy@Fe<sub>3</sub>O<sub>4</sub> NPs.

The variation in retention for a 20-ppm solution of uranyl ion with different quantities of Phy@Fe<sub>3</sub>O<sub>4</sub> NPs nanoparticles was studied next: 0.25, 0.5, 1, 1.5, 2, and 2.5 mg Phy@Fe<sub>3</sub>O<sub>4</sub> NPs were used. The capture percentages of U(VI) are all around 93% (Figure S6).

These tests used aerobic conditions without an inert atmosphere. Environmental carbon dioxide at pH  $\geq 8$  can be dissolved in the aqueous solution causing the formation of the complex  $[(\text{CO}_3)_2\text{UO}_2]^{4-}$  that reduces the retention percentages [22]. Nevertheless, this material has practical value in real environmental conditions. The retention of 100% of U(VI) is equivalent to a  $q_m$  of  $948 \pm 38$  mg milligrams of U(VI) per milligram of Phy@Fe<sub>3</sub>O<sub>4</sub> NPs used. This value is lower than others described in the literature [28] using magnetite nanoparticles with supported phosphate groups although the Phy@Fe<sub>3</sub>O<sub>4</sub> nanoparticles presented here differ from the others by showing a high affinity for cations Y(III) and Sr(II) that did impact their uptake of U(VI) for the simultaneous presence of both radioactive ions.

The Phy@Fe<sub>3</sub>O<sub>4</sub> NPs presented in this study are both effective and stable. When kept dry, they remain viable for more than three months with no loss of efficacy during subsequent uptake tests. Phosphonate coating causes a strong interaction with the surface of the magnetite and inhibit oxidation.

The TEM-EDS data of the decanted samples after use in the competitive capture of U(VI), Y(III), and Sr(II) are shown in Figure 9. In the orange box, the contamination due to the sample grid is highlighted. The green boxes show metals adsorbed on the surface of Phy@Fe<sub>3</sub>O<sub>4</sub> NPs. The red arrow indicates phosphorus and iron from Phy@Fe<sub>3</sub>O<sub>4</sub> NPs. These data confirm sorption effectiveness of Phy@Fe<sub>3</sub>O<sub>4</sub> NPs for these radioactive metals.

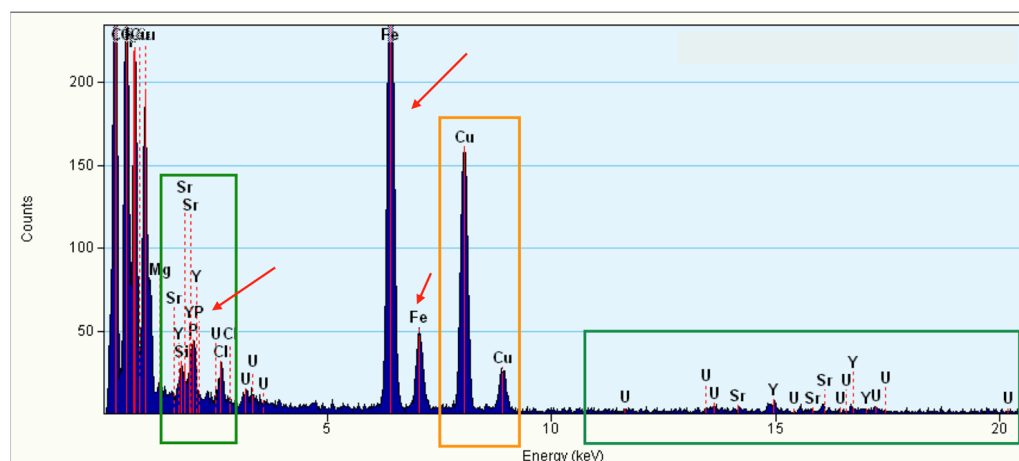


**Figure 9.** EDS spectrum acquired in TEM mode for a Phy@Fe<sub>3</sub>O<sub>4</sub>NPs sample. The orange boxes highlight the contributions from contamination on the sample grid, whereas the green box highlights the signal generated by the phosphate coating.

#### 4. Discussion

Many other papers have shown the recovery of U(VI), <sup>90</sup>Sr, and <sup>90</sup>Y salts. Table 2 shows a non-exhaustive list of adsorbent materials including removal or adsorption capacity, pH, and equilibrium time for optimal removal of U(VI), Sr(II), and Y(III). The results obtained here are also included.

Of the three cations studied here, the uranyl cation UO<sub>2</sub><sup>+</sup> has received the most attention from researchers. Therefore, different adsorbent materials of different origin have been described in the literature. Supramolecular receptors based on calixarenes [35–37] are particularly powerful as they are nanostructured porous materials, MOFs [38] recyclable chelating resins [39], polymeric chitosan functionalized with triethylene tetramine [40], porous polymers decorated with phytic acid [41], and some nanomaterials derived from iron oxide including magnetite functionalized with phosphate groups [34].

<sup>90</sup>Sr salt uptake has been described via crown ethers such as di-tert-butylidicyclohexano-18-crown-6 supported on magnetite or on maghemite [42–44]. Other systems include porous metal-organic frameworks (MOFs) [45–47], zeolites LTA (Linde Type A) [48], polymers of melanina [49], and derivatives of calixarenes (carboxy methoxy calix[6]arene [50] and thiocalix[4]arene diamide [51]).

The Y(III) salts can be eliminated from aqueous medium by precipitation with iron oxyhydroxide compounds [52]. Sorption on kaolinite [53], sodium alginate (99.01 mg/g) [54], or calcium alginate (181.81 mg/g) has been described. Nanomaghemite has been used effectively for removal of Y(III) salts (13.5 mg/g) [55].

The Phy@Fe<sub>3</sub>O<sub>4</sub> NPs presented here offers a high adsorption capacity at equilibrium ( $q_m$ ). The iron oxide nanomaterial adsorbs more U(VI) from an aqueous solution relative to the literature. To the best of our knowledge, the Phy@Fe<sub>3</sub>O<sub>4</sub> nanoparticles are the only receptors based on iron oxide described in the literature that can eliminate salts of U(VI), Y(III), and Sr(II) without interference.

**Table 2.** Comparison of U(VI), Sr(II), and Y(III) adsorption capacities reported for adsorbents in published studies and the material in this work.

Sorbent	Adsorption or Removal Performance	pH/Time	Ref.
<b>URANIUM</b>			
Biorecovery of uranium from aqueous solutions at the expense of phytic acid Fe <sub>3</sub> O <sub>4</sub> NPs (50–100 nm)	q <sub>m</sub> = 4.1 mg/g 75%	4.5/12 h	[56]
Phytic acid-decorated porous organic polymer for uranium extraction under highly acidic conditions Iminodiphosphonate functionalized PGMA–Fe <sub>3</sub> O <sub>4</sub> <sup>1</sup>	q <sub>m</sub> = 5 mg/g q <sub>m</sub> = 106.7 mg/g	7/5 h 5/11 h	[34] [41]
Triethylene tetramine functionalized chitosan resin–Fe <sub>3</sub> O <sub>4</sub>	q <sub>m</sub> = 147 mg/g q <sub>m</sub> = 166.6 mg/g	4–5/12 h 5/1 h	[57] [40]
Amidoxime functionalized flower-like TiO <sub>2</sub> microspheres–Fe <sub>3</sub> O <sub>4</sub>	q <sub>m</sub> = 313.6 mg/g	6/12 h	[58]
Graphene oxide modified with OPO <sub>3</sub> H <sub>2</sub> /mesoporous Zr-MOF–Fe <sub>3</sub> O <sub>4</sub>	q <sub>m</sub> = 416.7 mg/g	6.2/3 min	[59]
Diethylenetriamine Fe <sub>3</sub> O <sub>4</sub> -embedded mesoporous silica	q <sub>m</sub> = 470 mg/g	6/5 h	[60]
Phytic acid/polyaniline/FeOOH composites	q <sub>m</sub> = 555.8 mg/g (Removal efficiency = 92%)	8/5 min	[61]
Oleic acid bilayer@Fe <sub>3</sub> O <sub>4</sub> NPs	q <sub>m</sub> = 635 mg/g	5.6/24 h	[62]
Hydrothermal carbon modified with NaOH–Fe <sub>3</sub> O <sub>4</sub>	q <sub>m</sub> = 761.2 mg/g	5.5/200 min	[63]
Phytic acid doped polypyrrole/Carbon felt electrode	q <sub>m</sub> = 1562 mg/g (Removal efficiency = 98%)	5/8 h	[64]
Oleyl phosphate bilayer@MnFe <sub>2</sub> O <sub>4</sub> NPs	q <sub>m</sub> = 1667 mg/g	5.6/24 h	[65]
Phosphated-Fe <sub>3</sub> O <sub>4</sub> NPs	q <sub>m</sub> = 1690 mg/g (100%)	7/1 min	[24]
Phy@Fe <sub>3</sub> O <sub>4</sub> NPs	q <sub>m</sub> = 948 mg/g (Removal efficiency = 80%)	6.5/2 h	This work
<b>STRONTIUM</b>			
4',4''(5'')-di-tert-butylidicyclohexano-18-crown-6 onto Fe <sub>3</sub> O <sub>4</sub> @UiO-66-NH <sub>2</sub>	q <sub>m</sub> = 284 mL/g	1/90 min	[43]
γ-Fe <sub>2</sub> O <sub>3</sub> impregnated with 4',4''(5'')-di-tert-butylidicyclohexane 18-crown-6	(Removal efficiency = 66%)	7/10 min	[42]
Dicyclohexano-18-crown-6 ether impregnated titanate nanotubes	q <sub>m</sub> = 49 mg/g	1/180 min	[66]
MOF material	q <sub>m</sub> = 43.83 mg/g (Removal efficiency = 99,89%)	7/12 h	[47]
Ammonium molybdophosphate–polyacrylonitrile (AMP–PAN)	q <sub>m</sub> = 15 mg/g (Removal efficiency = 66%)	5/24 h	[67]
Phy@Fe <sub>3</sub> O <sub>4</sub> NPs	q <sub>m</sub> = 20 mg/g (Removal efficiency = 73%)	6.5/2 h	This work
<b>YTTRIUM</b>			
Nanomagemite	q <sub>m</sub> = 13.5 mg/g (Removal efficiency = 94%)	6.9/50 min	[55]
3-Amino-5-Hydroxypyrazole Impregnated Bleaching Clay	q <sub>m</sub> = 171.3 mg/g	6/60 min	[68]
Alginate compounds	q <sub>m</sub> = 99.01 mg/g (sodium alginate) q <sub>m</sub> = 181.81 mg/g (calcium alginate)	6/60 min	[54]
Kaolinite	q <sub>m</sub> = 0.029 mmol/g	5/3.5 h	[53]
Phy@Fe <sub>3</sub> O <sub>4</sub> NPs	q <sub>m</sub> = 20 mg/g (Removal efficiency = 100%)	6.5/2 h	This work

<sup>1</sup> PGMA: polyglycidyl methacrylate-magnetic nanocomposite.

## 5. Conclusions

In this work, a new hybrid material has been prepared and characterized. Phy@Fe<sub>3</sub>O<sub>4</sub> NPs has been obtained via conjunction of magnetite nanoparticles supported with phytate moieties. The new hybrid material is stable, affordable, and quick to prepare (3 min). The Phy@Fe<sub>3</sub>O<sub>4</sub> NPs show a high sorption capacity of the radioactive ions studied under real aerobic conditions. The system eliminates uranyl ions (100%), Y(III) (100%), and Sr(II) (73%) at pH 6.5, which is typical for most environmental samples.

Pristine magnetite nanoparticles, Fe<sub>3</sub>O<sub>4</sub> NPs, have a high surface reactivity and also show a quantitative sorption for U(VI), but much lower for Sr(II) (12%) and Y(III) (52%). Without post-coating, pristine magnetite nanoparticles are not stable, and a co-precipitation preparation method requires more synthetic effort and longer reaction times.

Phy@Fe<sub>3</sub>O<sub>4</sub> NPs are non-toxic and easily recovered via their magnetic characteristics. They are suitable for capturing dangerous radioactive substances. Due to their simplicity and versatility, the Phy@Fe<sub>3</sub>O<sub>4</sub> NPs have value in the circular economy. They can eliminate and confine dangerous radioactive metal ions such as <sup>90</sup>Sr, <sup>90</sup>Y, and (UO<sub>2</sub>)<sup>2+</sup> from water.

**Supplementary Materials:** The following supporting information can be downloaded at: <https://www.mdpi.com/article/10.3390/nano12244383/s1>, Figure S1. TEM micrograph, Dynamic light Scattering (DLS) analysis and Zeta Potential of Fe<sub>3</sub>O<sub>4</sub>NPs; Figure S2. FT-IR spectra of pristine magnetite nanoparticles; Figure S3. Thermogravimetric analysis (TGA) of pristine magnetite nanoparticles; Figure S4. Retention percentage of Sr(II) by Phy@Fe<sub>3</sub>O<sub>4</sub> NPs versus the initial concentration of Sr(II); Figure S5. Sr(II) retention percentage with different amounts of Phy@Fe<sub>3</sub>O<sub>4</sub> NPs; Figure S6. UO<sub>2</sub><sup>2+</sup> retention percentage with different amounts of Phy@Fe<sub>3</sub>O<sub>4</sub> NPs.

**Author Contributions:** Data curation, M.d.I.N.P. and P.D.; writing—original draft preparation, J.M.; writing—review & editing, P.D., M.d.I.N.P. and J.M. All authors have read and agreed to the published version of the manuscript.

**Funding:** The authors wish to thank Spanish Ministry of Economy, Industry and Competitiveness for funding project PID2020-115637GB-I00.

**Data Availability Statement:** Not applicable.

**Conflicts of Interest:** The authors declare no conflict of interest.

## References

1. USEPA. *National Primary Drinking Water Regulation; Radon-222; Proposed Rule*; USEPA: Washington, DC, USA, 1999.
2. Deuber, R.; Heim, T. Yttrium. In *Metals and Their Compounds in the Environment: Occurrence, Analysis and Biological Relevance*; Marian, E., Ed.; VCH: Weinheim, Germany, 1991; pp. 1299–1308.
3. USGS. Rare Earths—Scandium, Yttrium, and The Lanthanides. Available online: <https://www.usgs.gov/centers/national-minerals-information-center/rare-earths-statistics-and-information> (accessed on 15 September 2021).
4. Yttrium-90 Selective Internal Radiation Therapy (SIRT). Available online: <https://theranostics.sg/yttrium-90-selective-internal-radiation-therapy/> (accessed on 15 September 2021).
5. Radovic, M.; Mirkovic, M.; Peric, M.; Vukadinovic, A.; Stankovic, D.; Petrovic, D.; Boskovic, M.; Antic, B.; Markovic, M.; Vranjes-Duric, S. Design and preparation of <sup>90</sup>Y-labeled imidodiphosphate- and inositol hexaphosphatecoated magnetic nanoparticles for possible medical applications. *J. Mater. Chem. B* **2017**, *5*, 8738–8747. [[CrossRef](#)] [[PubMed](#)]
6. Mumma, R.O.; Raupach, D.C.; Sahadewan, K.; Manos, C.G.; Rutzket, M.; Kuntztt, H.T.; Bache, C.A.; Lisk, D.J. National survey of elements and radioactivity in municipal incinerator ashes. *Arch. Environ. Contam. Toxicol.* **1990**, *19*, 399–404. [[CrossRef](#)] [[PubMed](#)]
7. Sneller, F.E.C.; Kalf, D.F.; Weltje, L.; Van Wezel, A.P. Maximum Permissible Concentrations and Negligible Concentrations for Rare Earth Elements (REEs). June 2000. Available online: <https://inis.iaea.org/search/searchsinglerecord.aspx?recordsFor=SingleRecord&RN=31053152> (accessed on 15 September 2021).
8. Nielsen, S.P. The biological role of strontium. *Bone* **2004**, *35*, 583–588. [[CrossRef](#)] [[PubMed](#)]
9. Moon, J. The role of vitamin D in toxic metal absorption: A review. *J. Am. Coll. Nutr.* **1994**, *13*, 559–564. [[CrossRef](#)] [[PubMed](#)]
10. Uskokovic, V.; Uskokovic, D.P. (Eds.) *Nanotechnologies in Preventative and Regenerative Medicine*, 1st ed.; Elsevier: Amsterdam, The Netherlands, 2018.
11. Burger, A.A.; Lichtscheidl, I. Strontium in the environment: Review about reactions of plants towards stable and radioactive strontium isotopes. *Sci. Total Environ.* **2019**, *653*, 1458–1512. [[CrossRef](#)] [[PubMed](#)]
12. Phouthavong, V.; Yan, R.; Nijpanich, S.; Hagio, T.; Ichino, R.; Kong, L.; Li, L. Magnetic Adsorbents for Wastewater Treatment: Advancements in Their Synthesis Methods. *Materials* **2022**, *15*, 1053. [[CrossRef](#)]

13. Lu, W.; Li, J.; Sheng, Y.; Zhang, X.; You, J.; Chen, L. One-pot synthesis of magnetic iron oxide nanoparticle-multiwalled carbon nanotube composites for enhanced removal of Cr(VI) from aqueous solution. *J. Colloid Interface Sci.* **2017**, *505*, 1134–1146. [[CrossRef](#)]
14. Li, J.; Dong, R.; Wang, X.; Xiong, H.; Xu, S.; Shen, D.; Song, X.; Chen, L. One-pot synthesis of magnetic molecularly imprinted microspheres by RAFT precipitation polymerization for the fast and selective removal of 17 $\beta$ -estradiol. *RSC Adv.* **2015**, *5*, 10611–10618. [[CrossRef](#)]
15. Fuks, L.; Herdzik-Koniecko, I.; Polkowska-Motrenko, H.; Oszczak, A. Novel procedure for removal of the radioactive metals from aqueous wastes by the magnetic calcium alginate. *Int. J. Environ. Sci. Technol.* **2018**, *15*, 2657–2668. [[CrossRef](#)]
16. Duel, P.; Gutiérrez, M.S.; Rodríguez, P.; León, A.; López, K.A.; Morey, J.; Piña, M.N. Removal of Au<sup>3+</sup> and Ag<sup>+</sup> from aqueous media with magnetic nanoparticles functionalized with squaramide derivatives. *RSC Adv.* **2018**, *8*, 36123–36132. [[CrossRef](#)]
17. López, K.A.; Piña, M.N.; Quiñonero, D.; Ballester, P.; Morey, J. Highly efficient coordination of Hg<sup>2+</sup> and Pb<sup>2+</sup> metals in water with squaramide-coated Fe<sub>3</sub>O<sub>4</sub> nanoparticles. *J. Mater. Chem. A* **2014**, *2*, 8796–8803. [[CrossRef](#)]
18. Gutiérrez, M.S.; Duel, P.; Hierro, F.; Morey, J.; Piña, M.N. A very highly efficient magnetic nanomaterial for removal of PAHS from aqueous media. *Small* **2018**, *14*, 1702573. [[CrossRef](#)] [[PubMed](#)]
19. Piña, M.N.; Rodríguez, P.; Gutiérrez, M.S.; Quiñonero, D.; Morey, J.; Frontera, A. Adsorption and quantification of volatile organic compounds (VOCs) by using hybrid magnetic nanoparticles. *Chem. Eur. J.* **2018**, *24*, 12820–12826. [[CrossRef](#)] [[PubMed](#)]
20. Daou, T.J.; Grenèche, J.M.; Pourroy, G.; Buathong, S.; Derory, A.; Ulhaq-Bouillet, C.; Donnio, B.; Guillon, D.; Begin-Colin, S. Coupling agent effect on magnetic properties of functionalized magnetite-based nanoparticles. *Chem. Mater.* **2008**, *20*, 5869–5875. [[CrossRef](#)]
21. Yu, X.F.; Liu, Y.H.; Zhou, Z.W.; Xiong, G.X.; Cao, X.H.; Li, M.; Zhang, Z.B. Adsorptive removal of U(VI) from aqueous solution by hydrothermal carbon spheres with phosphate group. *J. Radioanal. Nucl. Chem.* **2014**, *300*, 1235–1244. [[CrossRef](#)]
22. Bachmaf, S.; Planer-Friedrich, B.; Merkel, B.J. Effect of sulfate, carbonate, and phosphate on the uranium (VI) sorption behavior onto bentonite. *Radiochim. Acta* **2008**, *96*, 359–366. [[CrossRef](#)]
23. Aly, M.M.; Hamza, F.M. A review: Studies on uranium removal using different techniques. Overview. *J. Dispersion Sci. Technol.* **2013**, *34*, 182–213. [[CrossRef](#)]
24. Cali, E.; Qi, J.; Preedy, O.; Chen, S.; Boldrin, D.; Branford, W.R.; Vandeperrea, L.; Ryan, M.P. Functionalised magnetic nanoparticles for uranium adsorption with ultra-high capacity and selectivity. *J. Mater. Chem. A* **2018**, *6*, 3063–3073. [[CrossRef](#)]
25. Park, H.; May, A.; Portilla, L.; Dietrich, H.; Münch, F.; Rejek, T.; Sarcletti, M.; Banspach, L.; Zahn, D.; Halik, M. Magnetite nanoparticles as efficient materials for removal glyphosate from water. *Nat. Sustain.* **2020**, *3*, 129–135. [[CrossRef](#)]
26. Torres, J.; Veiga, N.; Gancheff, J.S.; Domínguez, S.; Mederos, A.; Sundberg, M.; Sánchez, A.; Castiglioni, J.; Díaz, A.; Kremer, C. Interaction of myo-inositol hexakisphosphate with alkali and alkaline earth metal ions: Spectroscopic, potentiometric and theoretical studies. *J. Mol. Struct.* **2008**, *874*, 77–88. [[CrossRef](#)]
27. Brigando, C.; Mossoyan, J.C.; Favier, F.; Benlian, D. Conformational preferences and protonation sequence of myo-inositol hexaphosphate in aqueous solution; potentiometric and multinuclear magnetic resonance studies. *J. Chem. Soc. Dalt. Trans.* **1995**, *4*, 575–578. [[CrossRef](#)]
28. Veiga, N.; Torres, J.; MacHo, I.; Gómez, K.; González, G.; Kremer, C. Coordination, microprotonation equilibria and conformational changes of myo-inositol hexakisphosphate with pertinence to its biological function. *Dalton Trans.* **2014**, *43*, 16238–16251. [[CrossRef](#)] [[PubMed](#)]
29. Gui, L.; Chen, B.; Zhou, Z.; Liang, Y.; He, M.; Hu, B. Phytic acid functionalized magnetic adsorbents for facile enrichment of trace rare earth elements in environmental water, digested atmospheric particulates and the extracts followed by inductively coupled plasma mass spectrometry detection. *Talanta* **2022**, *244*, 123426. [[CrossRef](#)] [[PubMed](#)]
30. Yazdani, Y.; Seddigh, M. Magnetite nanoparticles synthesized by coprecipitation method: The effects of various iron anions on specifications. *Mater. Chem. Phys.* **2016**, *184*, 318–323. [[CrossRef](#)]
31. Mirabello, G.; Lenders, J.J.M.; Sommerdijk, N.A.J.M. Bioinspired synthesis of magnetite nanoparticles. *Chem. Soc. Rev.* **2016**, *45*, 5085–5106. [[CrossRef](#)]
32. Gutiérrez, M.S.; Piña, M.N.; Morey, J. Fast microwave-assisted conjugation of magnetic nanoparticles with carboxylates of biological interest. *RSC Adv.* **2017**, *7*, 19385–19390. [[CrossRef](#)]
33. Katsoyiannis, I.A.; Althoff, H.W.; Bartel, H.; Jekel, M. The effect of groundwater composition on uranium(VI) sorption onto bacteriogenic iron oxides. *Water Res.* **2006**, *40*, 3646–3652. [[CrossRef](#)]
34. Das, D.; Sureshkumar, M.K.; Koley, S.; Mithal, N.; Pillai, C.G.S. Sorption of uranium on magnetite nanoparticles. *J. Radioanal. Nucl. Chem.* **2010**, *285*, 447–454. [[CrossRef](#)]
35. Mokhtari, B.; Pourabdollah, K.; Dallali, D. A review of calixarene applications in nuclear industries. *J. Radioanal. Nucl. Chem.* **2011**, *287*, 921–934. [[CrossRef](#)]
36. Jung, J.; Cho, Y.H.; Hahn, P.S. Scavenging of UO<sub>2</sub><sup>2+</sup> using 4-sulfonic calix[6]arene in the presence of goethite. *J. Radioanal. Nucl. Chem.* **1999**, *242*, 635–639. [[CrossRef](#)]
37. Shinkai, S.; Koreishi, H.; Ueda, K.; Arimura, T.; Manabe, O. Molecular design of calixarene-based uranophiles which exhibit remarkably high stability and selectivity. *J. Am. Chem. Soc.* **1987**, *109*, 6371–6376. [[CrossRef](#)]
38. Carboni, M.; Abney, C.W.; Liu, S.; Lin, W. Highly porous and stable metal-organic frameworks for uranium extraction. *Chem. Sci.* **2013**, *4*, 2396–2402. [[CrossRef](#)]

39. Sather, A.C.; Berryman, O.B.; Rebek, J. Selective recognition and extraction of the uranyl ion from aqueous solutions with a recyclable chelating resin. *Chem. Sci.* **2013**, *4*, 3601–3605. [[CrossRef](#)]
40. Jin, J.; Huang, X.; Zhou, L.; Peng, J.; Wang, Y. In situ preparation of magnetic chitosan resins functionalized with triethylenetetramine for the adsorption of uranyl (II) ions. *J. Radioanal. Nucl. Chem.* **2015**, *303*, 797–806. [[CrossRef](#)]
41. Liang, L.; Zhang, H.; Lin, X.; Yan, K.; Li, M.; Pan, X.; Hu, Y.; Chen, Y.; Luo, X.; Shang, R. Phytic acid-decorated porous organic polymer for uranium extraction under highly acidic conditions. *Colloids Surf. A Physicochem. Eng. Asp.* **2021**, *625*, 126981. [[CrossRef](#)]
42. Shaikh, Y.; Lai, E.P.C.; Sadi, B.; Li, C. Magnetic nanoparticles impregnated with 18-crown-6 ether: Hybrid material synthesis for binding and detection of radioactive strontium. *Nanosci. Technol.* **2015**, *2*, 1–5.
43. Yin, L.; Kong, X.; Shao, X.; Ji, Y. Synthesis of DtBuCH18C6-coated magnetic metal–organic framework Fe<sub>3</sub>O<sub>4</sub>@UiO-66-NH<sub>2</sub> for strontium adsorption. *J. Environ. Chem. Eng.* **2019**, *7*, 103073. [[CrossRef](#)]
44. Songa, Y.; Dub, Y.; Lva, D.; Yea, G.; Wang, J. Macrocyclic receptors immobilized to monodisperse porous polymer particles by chemical grafting and physical impregnation for strontium capture: A comparative study. *J. Hazard. Mater.* **2014**, *274*, 221–228. [[CrossRef](#)]
45. Xiao, C.; Silver, M.A.; Wang, S. Metal–organic frameworks for radionuclide sequestration from aqueous solution: A brief overview and outlook. *J. Chem. Soc. Dalton Trans.* **2017**, *46*, 16381–16386. [[CrossRef](#)]
46. Li, J.; Wang, X.; Zhao, G.; Chen, C.; Chai, Z.; Alsaedi, A.; Hayat, T.; Wang, X. Metal–organic framework-based materials: Superior adsorbents for the capture of toxic and radioactive metal ions. *Chem. Soc. Rev.* **2018**, *47*, 2322–2356. [[CrossRef](#)]
47. Gao, Y.J.; Feng, M.L.; Zhang, B.; Wu, Z.F.; Song, Y.; Huang, X.Y. An easily synthesized microporous framework material for the selective capture of radioactive Cs<sup>+</sup> and Sr<sup>2+</sup> ions. *J. Mater. Chem. A* **2018**, *6*, 3967–3976. [[CrossRef](#)]
48. Kwon, S.; Choi, Y.; Singh, B.K.; Na, K. Selective and rapid capture of Sr<sup>2+</sup> with LTA zeolites: Effect of crystal sizes and mesoporosity. *Applied Surface Science* **2020**, *506*, 145029. [[CrossRef](#)]
49. Karabayira, E.; Ozdemirb, A.; Senkalc, B.F.; Taskind, O.S. A radioactively durable melamine-styrene based polymer: Highly efficient removal of <sup>90</sup>Sr. *Appl. Radiat. Isot.* **2019**, *149*, 96–103. [[CrossRef](#)]
50. Gupta, V.K.; Ludwig, R.; Agarwal, S. Strontium(II) sensor based on a modified calix[6]arene in PVC matrix. *Anal. Sci.* **2005**, *21*, 293–296. [[CrossRef](#)] [[PubMed](#)]
51. Kim, T.H.; Kim, H.; Lee, J.H.; Kim, J.S. Sr<sup>2+</sup> ion selective p-tert-butylthiacalix[4]arene bearing two distal amide units. *Bull. Korean. Chem. Soc.* **2008**, *29*, 620–622.
52. Bau, M. Scavenging of dissolved yttrium and rare earths by precipitating iron oxyhydroxide: Experimental evidence for Ce oxidation, Y-Ho fractionation, and lanthanide tetrad effect. *Geochimica Cosmochimica Acta* **1999**, *63*, 67–77. [[CrossRef](#)]
53. Zhou, F.; Feng, J.; Xie, X.; Wu, B.; Liu, Q.; Wu, X.; Chi, R. Adsorption of lanthanum (III) and yttrium (III) on kaolinite: Kinetics and adsorption isotherms. *Physicochem. Probl. Miner. Process.* **2019**, *55*, 928–939.
54. Khotimchenko, M.; Kovalev, V.; Khozhaenko, E.; Khotimchenko, R. Removal of yttrium (III) ions from water solutions by alginate compounds. *Int. J. Environ. Sci. Technol.* **2015**, *12*, 3107–3116. [[CrossRef](#)]
55. Dubey, S.; Grandhi, S.S. Sorption studies of yttrium (III) ions on nanomagemite. *J. Environ. Chem. Eng.* **2016**, *4*, 4719–4730. [[CrossRef](#)]
56. Innocenzi, V.; De Michelis, I.; Kopacek, B.; Vegliò, F. Yttrium recovery from primary and secondary sources: A review of main hydrometallurgical processes. *Waste Manag.* **2014**, *34*, 1237–1250. [[CrossRef](#)]
57. Galhoum, A.A. Facile synthesis of functionalized polyglycidyl methacrylate-magnetic nanocomposites for enhanced uranium sorption. *RSC Adv.* **2019**, *9*, 38783–38796. [[CrossRef](#)] [[PubMed](#)]
58. Zhao, M.; Cui, Z.; Pan, D.; Fan, F.; Tang, J.; Hu, Y.; Xu, Y.; Zhang, P.; Li, P.; Kong, X.Y. An efficient uranium adsorption magnetic platform based on amidoxime-functionalized flower-like Fe<sub>3</sub>O<sub>4</sub>@TiO<sub>2</sub> core-shell microspheres. *ACS Appl. Mater. Interfaces* **2021**, *13*, 17931–17939. [[CrossRef](#)] [[PubMed](#)]
59. Amini, A.; Khajeh, M.; Oveisi, A.R.; Daliran, S.; Ghaffari-Moghaddam, M.; Delarami, H.S. A porous multifunctional and magnetic layered graphene oxide/3D mesoporous MOF nanocomposite for rapid adsorption of uranium(VI) from aqueous solutions. *J. Ind. Eng. Chem.* **2021**, *93*, 322–332. [[CrossRef](#)]
60. Amesh, P.; Venkatesan, K.A.; Suneesh, A.S.; Gupta, D.K.; Ravindrana, T.R. Adsorption of uranium by diethylenetriamine functionalized magnetic mesoporous silica. *Environ. Nanotechnol. Monit. Manag.* **2021**, *16*, 100583. [[CrossRef](#)]
61. Wei, X.; Liu, Q.; Zhang, H.; Liu, J.; Chen, R.; Li, R.; Li, Z.; Liu, P.; Wang, J. Rapid and efficient uranium(VI) capture by phytic acid/polyaniline/FeOOH composites. *J. Colloid Interface Sci.* **2018**, *511*, 1–11. [[CrossRef](#)]
62. Li, W.; Troyer, L.D.; Lee, S.S.; Wu, J.; Kim, C.; Lafferty, B.J.; Catalano, J.G.; Fortner, J.D. Engineering nanoscale ironoxides for uranyl sorption and separation: Optimization of particle core size and bilayer surface coatings. *ACS Appl. Mater. Interfaces* **2017**, *9*, 13163–13172. [[CrossRef](#)]
63. Lai, Z.; Xuan, Z.; Yu, S.; Zhang, Z.; Cao, Y.; Zhao, Y.; Li, Y.; Luo, J.; Li, X. Synthesis of magnetic-carbon sorbent for removal of U(VI) from aqueous solution. *J. Radioanal. Nucl. Chem.* **2019**, *322*, 2079–2089. [[CrossRef](#)]
64. Huang, J.; Liu, Z.; Huang, D.; Jin, T.; Qian, Y. Efficient removal of uranium (VI) with a phytic acid-doped polypyrrole/carbon felt electrode using double potential step technique. *J. Hazard. Mater.* **2022**, *433*, 128775. [[CrossRef](#)]
65. Lee, S.S.; Li, W.; Kim, C.; Cho, M.; Lafferty, B.J.; Fortner, J.D. Surface functionalized manganese ferrite nanocrystals for enhanced uranium sorption and separation in water. *J. Mater. Chem. A* **2015**, *3*, 21930–21939. [[CrossRef](#)]

66. Ma, J.; Zhang, Y.; Ouyang, J.; Wu, X.; Luo, J.; Liu, S.; Gong, X. A facile preparation of dicyclohexano-18-crown-6 ether impregnated titanate nanotubes for strontium removal from acidic solution. *Solid State Sci.* **2019**, *90*, 49–55. [[CrossRef](#)]
67. Younjlin, P.; Youngchae, L.; Wonsik, S.; Sangjune. Removal of cobalt, strontium and cesium from radioactive laundry wastewater by ammonium molybdophosphate-polyacrylonitrile (AMP-PAN). *Chem. Eng. J.* **2010**, *162*, 685–695.
68. Sakr, A.K.; Cheira, M.F.; Hassanin, M.A.; Mira, H.I.; Mohamed, S.A.; Khandaker, M.U.; Hamid Osman, H.; Eed, E.M.; Sayyed, M.I.; Hanfi, M.Y. Adsorption of yttrium ions on 3-amino-5-hydroxypyrazole impregnated bleaching clay, a novel sorbent material. *Appl. Sci.* **2021**, *11*, 10320. [[CrossRef](#)]